



## Article

# Ecological Sorption of Iron and Sulfate Ions onto Starch and Chitosan Biopolymer Blend

Rahma Boughanmi, Christine Steinbach, Niklas Gerlach, Marina Oelmann, Christoph Beutner and Simona Schwarz \*

Leibniz-Institut für Polymerforschung Dresden e.V., Hohe Str. 6, 01069 Dresden, Germany; boughanmi@ipfdd.de (R.B.); steinbach@ipfdd.de (C.S.); gerlach@ipfdd.de (N.G.); oelmann@ipfdd.de (M.O.); beutner@ipfdd.de (C.B.)

\* Correspondence: simsch@ipfdd.de; Tel.: +49-351-46-58-333

**Abstract:** Providing safe drinking water free of heavy metal ions like iron and oxyanions like sulfate has become a worldwide issue. Starch, as one of the widely cheapest and available biomaterials, has demonstrated its capability to adsorb heavy metal ions from water in various scientific research, but in low adsorption rates. Therefore, this paper aims to prepare a biopolymer based on a starch–chitosan blend to raise the adsorption efficiency of starch. Two types of chitosan were used to modify potato starch (ps): low molecular chitosan (ch60) and high molecular chitosan (ch4000). Nano potato starch (n.ps) was prepared from potato starch and was also modified with both chitosans. The surface property, the morphology, the particle size, and the structure of the samples were analyzed. Moreover, the investigation of the samples by the zeta potential and charge density were evaluated to determine the charge of the adsorbents' surface. Furthermore, the pseudo first order (PFO) and pseudo second order (PSO) were employed to examine the adsorption kinetic. The adsorption isotherms of  $\text{Fe}^{2+/3+}$  and  $\text{SO}_4^{2-}$  were fitted employing Langmuir, Sips, and Dubinin-Radushkevich adsorption models. The maximum achieved sorption capacities from the  $\text{FeSO}_4$  solution for  $\text{Fe}^{2+/3+}$  were as follows: 115 mg/g for n.ps & ch4000, 90 mg/g for ps & ch4000, 80 mg/g for n.ps & ch60, and 61 mg/g for ps & ch60. Similarly, for  $\text{SO}_4^{2-}$ , it was 192 mg/g for n.ps & ch4000, 155 mg/g for n.ps & ch60, 137 mg/g for ps & ch4000, and 97 mg/g for ps & ch60.

**Keywords:** native starch; nano starch; chitosan; adsorption; heavy metal ions; iron ions; sulfate ions; water contamination



**Citation:** Boughanmi, R.; Steinbach, C.; Gerlach, N.; Oelmann, M.; Beutner, C.; Schwarz, S. Ecological Sorption of Iron and Sulfate Ions onto Starch and Chitosan Biopolymer Blend. *Polysaccharides* **2023**, *4*, 325–342. <https://doi.org/10.3390/polysaccharides4030019>

Academic Editor: Edson C. Silva-Fiho

Received: 23 July 2023

Revised: 6 September 2023

Accepted: 9 September 2023

Published: 12 September 2023



**Copyright:** © 2023 by the authors. Licensee MDPI, Basel, Switzerland. This article is an open access article distributed under the terms and conditions of the Creative Commons Attribution (CC BY) license (<https://creativecommons.org/licenses/by/4.0/>).

## 1. Introduction

The rising levels of iron- and sulfate ions in surface water sources can be attributed to various factors, including the expansion of industrial activities, agricultural runoff, and inadequate waste management practices. This situation has raised a worldwide awareness about water quality, emphasizing the urgent need to develop effective solutions for providing clean surface water. Indeed, various countries globally suffer from the shortage of fresh water and global drought conditions, due to climate change and declining precipitation levels. All these pressing issues currently confronting humanity underscore the urgent need for effective solutions to prevent their further exacerbation. Water contamination by iron ions is a problem originating either from natural causes or human activities, including industrial waste and acid mine drainage [1].

Iron is an essential element for the growth of nearly all living organisms [2]. However, excess consumption can lead to chronic disorders such as heart disease and cancer. This is particularly prevalent in patients with genetic predispositions towards excessive iron accumulation [3]. Furthermore, the presence of iron ions in water can alter the watercolor to a rusty-brown and affect its taste.

On the other hand, sulfate ions are commonly found in groundwater, fresh water, and surface water. Sulfate water contamination can result from natural processes, like mineral

weathering, volcanic activity, the breakdown and combustion of organic compounds, sulfide oxidation, and sea spray aerosols, as well as human activities such as acid mine drainage [4,5]. Elevated concentrations of sulfate ions in water could cause a human health risk, as they may be present in lakes up to 250 mg/L [4,6]. A promising strategy to mitigate this crisis involves the employment of biopolymers, specifically chitosan and starch, for the treatment of contaminated surface water.

Starch is a natural biopolymer that comprises two chains: (1) amylose, a linear chain connected via  $\alpha$ -1,4 glycosidic bonds, and (2) amylopectin, a branched chain incorporating the  $\alpha$ -1,6 glycosidic linkages alongside the  $\alpha$ -1,4 type [7]. Starch was used as an adsorber of heavy metal ions owing to its biodegradability, ecofriendly, nature availability, and low cost. Yet, native starch exhibits low adsorption capacities towards heavy metal ions, and no adsorption of sulfate ions, which has been proven in our previous works [8,9]. Chitosan, a derivative of chitin, stands as the second most abundant biopolymer after cellulose [10] and displays high adsorption capacities towards heavy metal ions like iron and sulfate ions owing to its structure, as it is a copolymer of D-glucosamine and N-acetylglucosamine connected by 1,4-glycosidic linkages. With benefits such as biodegradability, biocompatibility, antibacterial properties, and high adsorption capacities, chitosan has garnered increasing attention in water treatment applications. However, the relative expense of chitosan compared to starch influences its use on an industrial scale [11–13].

The objective of this study is to blend starch with chitosan to enhance the adsorption of heavy metal ions and to reduce chitosan costs by decreasing the chitosan quantity and substituting part of the starch with chitosan. However, there is a limited number of studies that have explored the preparation of starch–chitosan blends for use as adsorbent materials in the removal of heavy metal ions [14,15], as conducted by S. Ramasubramaniam et al. These binary polymer blends were formulated by combining chitosan and starch in a 1:1 ratio, with and without the addition of glutaraldehyde as a cross-linking agent. The results from this research demonstrate the exceptional adsorption capabilities of the chitosan–starch blend, particularly in the context of cadmium (II) ion removal. Another study, led by Atangana et al., presents findings on the synthesis and characterization of cross-linked chitosan–starch composites derived from crab and shrimp shells. Furthermore, this investigation examines the effects of ten distinct cross-linking polymers, including glutaraldehyde, formaldehyde, epichlorohydrin, maleic anhydride, p-benzoquinone, poly(ethylene) glycol diglycidyl ether (PEG diglycidyl ether), 1-vinyl-2-pyrrolidone, 1,3-dichloroacetone, acrylic acid, and s-methyl-benzylamine in the formulation process. The products were characterized using FT-IR and SEM images.

This study investigates the modification of native and nano potato starch with the cheapest, faster, and most ecofriendly method using chitosan. Two different types of chitosan flakes were used: a long-chain chitosan and a short-chain chitosan. Firstly, native potato starch was modified with both chitosan types. After that, to examine the effect of particle size of the modified starch with chitosan, nano potato starches were synthesized. These nano starches were modified once with the long-chain chitosan and once with the short-chain chitosan. To analyze the surface properties and the morphologies of the studied particles' SEM, SEM-EDX before and after the adsorption was employed. To determine the functional groups of the tested adsorbents, ATR-FTIR and the particle charge distribution were used. To determine the particle size, Laser Diffraction and DLS were employed. The adsorption isotherms' kinetics of iron and sulfate ions were studied and evaluated by the Pseudo-First-Order (PFO) and Pseudo-Second-Order (PSO). Herein, Langmuir, Sips, and Dubinin–Radushkevich fitting models were applied to fit the adsorption isotherms.

## 2. Materials and Methods

### 2.1. Materials

Native potato starch 4757 (ps) was provided from Agrana GmbH; low molecular weight chitosan 90/60/A1 (ch60) and high molecular weight chitosan 90/4000/A1 (ch4000) were provided from BioLog Heppe GmbH®. The indices of 90 indicate the degree of

deacetylation (DD) in %, 60 and 4000 correspond to viscosity in mPas, and A1 signifies 1% ash. The used samples for the adsorption were cited in Table 1.

**Table 1.** Samples and their used codes in the text.

Element 1	Element 2	Ratio	Sample Code
Chitosan 90/60/A1	-	-	ch60
Chitosan 90/4000/A1	-	-	ch4000
Native potato starch	-	-	ps
Nano potato starch	-	-	n.ps
Chitosan 90/60/A1	Native potato starch	1:1	ps & ch60
Chitosan 90/4000/A1	Native potato starch	1:1	ps & ch4000
Chitosan 90/60/A1	Nano potato starch	1:1	n.ps & ch60
Chitosan 90/4000/A1	Nano potato starch	1:1	n.ps & ch4000

Acetic acid from Merck KGaA in Darmstadt in Germany was acquired to solve the chitosan. Acetone and methanol were acquired from VWR (99%) from Darmstadt in Germany, and iron sulfate  $\text{FeSO}_4 \cdot 7\text{H}_2\text{O}$  (99%) was purchased from Sigma Aldrich from Munich in Germany.

For all experiments, we used ultrapure water using a Milli-Q Advantage A10<sup>®</sup> from Darmstadt in Germany characterized by TOC 5 ppb, and resistivity  $18.2 \text{ M}\cdot\text{cm}^{-1}$  was utilized to obtain ultrapure water.

#### 2.1.1. Synthesis of Starch Chitosan Blend

The synthesis of starch modified with chitosan is based on Reis et al. [16]. In an 800 mL beaker containing 350 mL acetic acid (0.12 M), 2.6 g of chitosan and 2.6 g of either native potato starch or nano potato starch were dispersed over one day. After the complete dissolution of chitosan, the pH of the solution was then adjusted dropwise and slowly until pH 7.0 using an NaOH solution (2 M). Then, the mixture was stirred until the next day. The pH was checked and readjusted to pH 7.0 if necessary.

After reaching a stable pH, the solution was precipitated for about 3 h in approximately 2 L of acetone, aspirated with a Büchner funnel, a water jet pump, and filtered with a sartorius filter “388” and then the precipitate was washed with 0.5 L of hot methanol. Lastly, the precipitate was dried for 15 h at 50 °C using a drying cabinet.

#### 2.1.2. Synthesis of Nano Potato Starch

In an oil bath with a temperature of 100 °C, 6 g of starch was dissolved in water and stirred. After one hour of stirring, 1 L of ethanol was added drop-wise. The solution was centrifuged at 4700 rpm for a duration of 20 min. The precipitate was decanted and then dried at 50 °C overnight using a drying cabinet.

### 2.2. Methods

**Scanning Electron Microscope (SEM):** The surface morphology of the samples was investigated using SEM. A scanning electron microscope Ultra plus (SEM) from Carl Zeiss Microscopy GmbH from Oberkochen in Germany was used. Before the measurements started, the samples were adhered to an aluminum pin sample tray using double-sided adhesive carbon tape. Then,  $\text{N}_2$  was flowed to obtain only a thin layer of particles, using a Sputter Coater SCD050 from Leica Microsystems from Wetzlar in Germany. The particles were coated using platinum. Eventually, the experiments were performed at different magnifications using a 3 keV acceleration voltage.

**Thermogravimetric analysis (TGA):** Using a Mettler Toledo 1 Star System from Gießen in Germany, (TGA) was performed. In a platinum crucible, the measurements were performed using around 5 mg to 7 mg of samples. The temperature range under investigation was 30 °C to 1000 °C, using flow rates of 40 mL/min and heating rates of 10 °C/min in  $\text{N}_2$  atmospheres.

Attenuated total reflection infrared Spectroscopy (ATR-FTIR): All samples were analyzed in the dry state using a resolution of  $2\text{ cm}^{-1}$  and 100 scans. The ATR-FTIR spectra were performed using a Tensor 27 equipment and a Platinum ATR module from the Bruker Corporation (Billerica, MA, USA).

Energy Dispersive Spectroscopy (SEM-EDX): The samples were analyzed employing a Phenom XL Workstation provided by Thermo Scientific from Waltham in USA equipped by a  $25\text{ mm}^2$  silicon drift detector (SDD), incorporating a thermoelectric cooling system (LN<sub>2</sub>-free) energy-dispersive X-ray spectroscopy (EDX) detector.

The particles were adhered to an aluminum pin sample tray. The tests were performed at various magnifications using a low-pressure mode ( $p = 60\text{ Pa}$ ) and a 15 keV acceleration voltage.

pH Measurement: The device SevenExcellence purchased by Mettler Toledo from Gießen in Germany was used to determine the pH values of the samples. The measures were performed at room temperature.

Streaming Potential and Charge Density: The measurements were carried out to identify the functional groups of the samples. An amount of 12.5 mg of the synthesized particles, including both chitosan and starch particles, were weighed in a 250 mL volumetric flask. An amount of 180 mL of Milli-Q water and 5 mL of acetic acid were added to each flask. After 2 h of stirring, the pH of each solution was adjusted to pH 1, 3, and 5. Then, 10 mL of water was added, and the pH was readjusted to 1, 3, and 5. After 24 h of stirring, the charge densities and streaming potential were measured using the particle charge detector (PCD04) from Mütek Analytik GmbH from Herrsching in Germany. The charge density of the positively charged samples was measured using an anionic titrant PES-Na (0.001 M), and the negatively charged samples were measured using a cationic titrant P-DADAMAC (0.001 M). The streaming potential was measured using NaOH (0.1 M) for pH ranges from 5 to 9 and HCL (0.1 M) for pH ranges from 5 to 3.

Nitrogen Sorption Isotherm: The measurements were carried out with the Autosorb iQMP from Quantachrome Instruments from Boynton Beach in USA. The studied samples were dried in a vacuum oven at  $100\text{ }^\circ\text{C}$ . The samples were activated by degassing in the vacuum ( $5 \times 10^{-10}\text{ mbar}$ ) at  $80\text{ }^\circ\text{C}$ . The experiments were carried out at  $77\text{ K}$ .

Dynamic Light Scattering (DLS): The particle size distribution of the samples' DLS was measured using a Zetasizer ZS device from Malvern Panalytical GmbH (Kassel, Germany). N.p.s suspension was prepared from the 10 mg sample and 30 mL Milli-Q water, stirred for 24 h, and then mixed using sonotrode for 10 s.

A Laser Diffractometry Mastersizer 3000 was used to determine the Particle size distribution of starch–chitosan blends. The instrument was purchased from Malvern Panalytical GmbH from Kassel in Germany. For the measurements, the dry chitosan particles and the starch–chitosan blends were directly introduced into the dispersion chamber, stirred for 5 min by 2000 rpm, and subsequently measured.

Centrifugation was performed to separate the supernatants. A 3-18KS centrifuge from Sigma Laborzentrifugen from Osterode am Harz in Germany was used. The samples were centrifuged at 11,000 rpm for 10 min.

Inductively Coupled Plasma Optical Emission Spectroscopy (ICP-OES): To determine the concentration of the different samples before and after adsorption, ICP-OES was used. An ICP-OES (iCAP 7000 Plus acquired from Thermo Fischer Scientific, from Darmstadt in Germany was used, and for the preservation of the samples, HNO<sub>3</sub> (65%, Normapur®) purchased from VWR from Darmstadt in Germany was used.

### 2.3. Adsorption Experiments

#### 2.3.1. Adsorption in Dependence on Time

To investigate the adsorption kinetics over time, a stock solution of FeSO<sub>4</sub> was prepared with a starting concentration of  $1000\text{ mg Fe}^{2+/3+}/\text{L}$ . Here, 30 mL was added in 50 mL centrifuge tubes containing 0.1 g of blends for different times ranging from 5 min to 24 h. Following stirring, the investigated blends were centrifuged for 10 min with 11,000 rpm. Subsequently, 8 mL of the resulting supernatants were introduced into 15 mL centrifuge

tubes. Finally, 2 mL of 20 wt% nitric acid were added for preservation. The concentrations of  $\text{Fe}^{2+/3+}$  and  $\text{SO}_4^{2-}$  ions were determined by ICP-OES.

### 2.3.2. Adsorption Isotherms

The stock solutions used in the adsorption tests were created in volumetric flasks by dissolving the respective salts in ultrapure water. For the tests, 0.1 g of the starch–chitosan samples were placed in a 50 mL centrifuge tube to which 30 mL of the  $\text{FeSO}_4$  solution was added. The mixture was stirred for 2 h and then centrifuged for 10 min at 11,000 rpm. Next, 8 mL of the resultant supernatant was moved to 15 mL centrifuge tubes, with 2 mL of 20 wt% nitric acid being added to preserve the samples. The concentrations of the  $\text{Fe}^{2+}$  and  $\text{SO}_4^{2-}$  ions were then determined using ICP-OES.

## 3. Theory Part

### 3.1. Adsorption Test

The concentration rates, Equation (1), and the concentration capacity, Equation (2), of the samples were calculated as follows:

$$\text{Adsorption in \%} = \frac{c_0 - c_{eq}}{c_0} \times 100 \quad (1)$$

$$q \text{ in } \text{mg} \cdot \text{g}^{-1} = \frac{c_0 - c_{eq}}{m} \times V \quad (2)$$

$c_0$  is the initial concentration at  $t = 0$ ,  $c_{eq}$  is the equilibrium concentration,  $q$  the adsorption capacity,  $m$  is the mass of samples in g, and  $V$  is the volume in L.

### 3.2. Kinetic Isotherms

The kinetic model provides information about the mass transfer mechanisms, the adsorbents effectiveness, and the adsorption rate [17,18].

To describe the kinetics of the studied isotherms in this paper, two kinetic models were used: the pseudo first order (PFO) proposed by Lagergren in 1898 [19,20],

$$q_t = q_{eq} \times (1 - e^{-k_1 t}), \quad (3)$$

and the pseudo second order (PSO) applied for the first time by Ho et al. [19,21],

$$q_t = \frac{q_{eq}^2 \times k_2 \times t}{1 + q_{eq} k_2 t} \quad (4)$$

$q_{eq}$  is the sorption capacities at equilibrium and  $q_t$  is the sorption capacities at time  $t$ ;  $k_1$  is the rate constant of pseudo-first-order sorption, and  $k_2$  is the rate constant of pseudo-first-order sorption [22].

### 3.3. Adsorption Isotherms

Sips, Langmuir, and Dubinin–Radushkevich as nonlinear isotherm fittings were used to model the sorption isotherms of iron sulfate onto modified starch.

Langmuir model [23]:

$$q_{eq} = \frac{Q_m \times K_L \times c_{eq}}{1 + K_L \times c_{eq}} \quad (5)$$

Sips model [24]:

$$q_{eq} = \frac{Q_m \times K_S \times c_{eq}^n}{1 + K_S \times c_{eq}^n} \quad (6)$$

Dubinin–Radushkevich [25]:

$$q_{eq} = Q_m \times \exp(-\beta_{DR} \times \varepsilon^2) \quad (7)$$

$$\varepsilon = RT \times \ln \left( 1 + \frac{1}{C_{eq}} \right) \quad (8)$$

$$E_{ads,DR} = \frac{1}{\sqrt{2 \times \beta_{DR}}} \quad (9)$$

$Q_m$  represents the maximum adsorption capacity,  $K_L$  corresponds to the Langmuir parameter,  $K_s$  corresponds to the Sips parameter,  $C_{eq}$  is the equilibrium concentration,  $n$  is the Sips model exponent,  $\beta_{DR}$  is the activity coefficient,  $E_{ads,DR}$  corresponds to the mean free energy of adsorption, and  $\varepsilon$  corresponds to the Polanyi potential [26,27].

## 4. Results and Discussion

### 4.1. Characterization of Starch–Chitosan Blends

In this section, we identify the functional groups present in the particles, and determine their charges to better understand the interactions occurring between the chitosan and starch particles. Specifically, we investigated the charge density and streaming potential, with consideration for the particles' pH. For these assessments, we used a particle charge detector PCD 04 provided by the Müttek company. The corresponding method was described in Section 2.2.

Figure 1 depicts the streaming potential curves and the charge density diagram for ch60 and ch4000. Notably, these curves exhibit a positive streaming potential within the acidic pH ranges of 3 to 6.5, attributable to the presence of amino groups. As the pH increases, the streaming potential decreases gradually due to the deprotonation of the amino groups within this pH range [28]. This continues until it reaches the isoelectric point (IEP) at pH 6.5. Following this, the charge transitions from positive to negative within basic pH ranges, ultimately reaching a plateau.

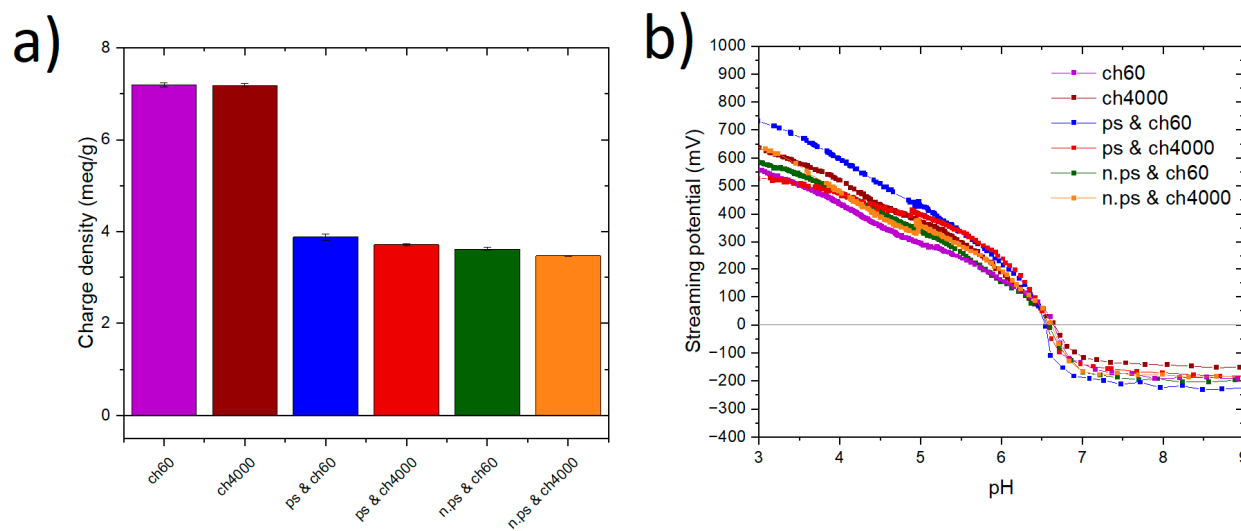


**Figure 1.** (a) Charge densities of the different studied particles at pH 5. (b) Streaming potential vs. pH from pH 3 until pH 9 of ch60 (purple), ps & ch60 (dark blue), n.ps & ch60 (green), ch4000 (brown), ps & ch4000 (red), and n.ps & ch4000 (orange). The respective charge densities of the different studied particles at pH 1 and pH 3 were presented in Figure S1.

In Figure 1 and Figure S1 in Supplementary Materials, we measured the charge density of different samples at pH 1, pH 3, and pH 5. In Figure 1, the charge density diagram shows that both chitosans were highly positively charged at pH 5, similar to pH 1 and pH 3 in Figure S1. Both ch60 and ch4000 had high charge densities of 7.2 meq/g and 7.1 meq/g, respectively. This strong positive charge is because of the abundance of amine groups.

The polycationic polymer chitosan with amine groups exhibits a positive charge when deprotonated in water ( $\text{NH}_3^+$ ). This positive charge enables chitosan to interact with negatively charged ions like ( $\text{SO}_4^{2-}$ ) through electrostatic attraction. Furthermore, it facilitates the subsequent adsorption of positively charged ions ( $\text{Fe}^{2+/3+}$ ) from the solution. The amino groups on the chitosan's surface act as binding sites for these ions. Moreover, due to the presence of weak ligand bases such as  $\text{NH}_2$  and  $\text{OH}$  groups in the chemical structure of the adsorbers, the weak Lewis acids of  $\text{Fe}^{2+/3+}$  form a stable complex with the chitosan.

On the other hand, starch contains hydroxyl groups that aid in the adsorption of  $\text{Fe}^{2+/3+}$  ions. These hydroxyl groups provide additional surface area and interaction sites for the adsorbate. Starch essentially acts as a supporting component, enhancing the available surface for adsorption.

When chitosan and starch are blended together, we observe a synergistic effect. This synergy often results in an enhanced adsorption capacity compared to using either component individually. However, it is essential to note that in our specific case, the presence of starch can lead to competition between starch molecules and the adsorbate for adsorption sites on the chitosan component. This competitive aspect was considered in our experimental design.

The decision to include starch in the blend was influenced by several factors, including cost optimization. Chitosan is relatively more expensive than starch, so by incorporating starch, we aimed to achieve effective adsorption while optimizing overall costs.

When native and nano starch with chitosans were blended, there was a noticeable decrease in charge densities. For the ps & ch60 and ps & ch4000 samples, charge densities dropped to 3.7 meq/g and 3.6 meq/g, respectively, and their IEPs were lower than those of the native chitosans. This decrease in charge density is due to the presence of starch, which has hydroxyl groups that give it a negative charge. Starch has a negative charge from pH 3 to pH 9, suggesting the possibility of hydrogen bonds forming between chitosan's amine and hydroxyl groups and starch's hydroxyl groups [29]. At these pH values, the amine groups of chitosan are protonated to  $\text{NH}_3^+$ , which may cause ionic interaction between starch and chitosan.

On the other hand, the introduction of starch results in the formation of agglomerated particles, due to the mixing of both chitosan and starch together, which may pose difficulties to detect the charge of the particles.

The addition of nanoscale potato starch to both chitosans resulted in a decrease of charge densities. This suggests that due to the presence of nanometric starch, smaller particles are present on the surface, leading to an increase in the negative charge.

The elemental analysis of the studied samples was conducted, and the results are presented in Table 2. As expected, and in line with our previous work [9], starch contains no nitrogen, implying the absence of proteins. Both types of chitosans contain 7.51% and 7.49% nitrogen, respectively, because of the presence of amino groups into the chain. The nitrogen content in the ps & ch60, ps & ch4000, n.ps & ch60, and n.ps & ch4000 samples is reduced by half, attributable to the 1:1 ratio of chitosan to starch.

**Table 2.** Results of the elemental analysis of the different samples used for the adsorption.

Sample	C (wt%)	H (wt%)	N (wt%)	Residue (wt%)
ch60	40.86	6.81	7.49	44.84
ch4000	41.25	6.77	7.51	44.47
ps	38.32	5.32	0.0	56.36
ps & ch60	41.01	6.63	3.63	48.73
ps & ch4000	40.40	6.58	3.93	49.09
n.ps & ch60	41.27	6.59	3.78	48.36
n.ps & ch4000	40.82	6.54	3.42	49.22

The samples were examined using ATR-FTIR spectroscopy to determine their functional groups and their chemical structure (see Figure 2). All samples show almost similar bands. Both chitosans ch60 and ch4000 showed similar vibrations; the broad peak at  $3350\text{ cm}^{-1}$  was ascribed to the stretching vibration of OH, NH, and the intermolecular hydrogen bonding; the Peak at  $2871\text{ cm}^{-1}$  was ascribed to the  $-\text{CH}$  bending ( $-\text{CH}$  from  $-\text{NHCOCH}_3$ ) [14]. The band at  $2920\text{ cm}^{-1}$  and  $2871\text{ cm}^{-1}$  confirm the presence of symmetric and asymmetric stretching vibrations of  $\text{CH}_2$  [30]. The stretching vibration of the CO bonds in the amide group  $\text{RNHCO}$  are described by the peak at  $1648\text{ cm}^{-1}$  [15].

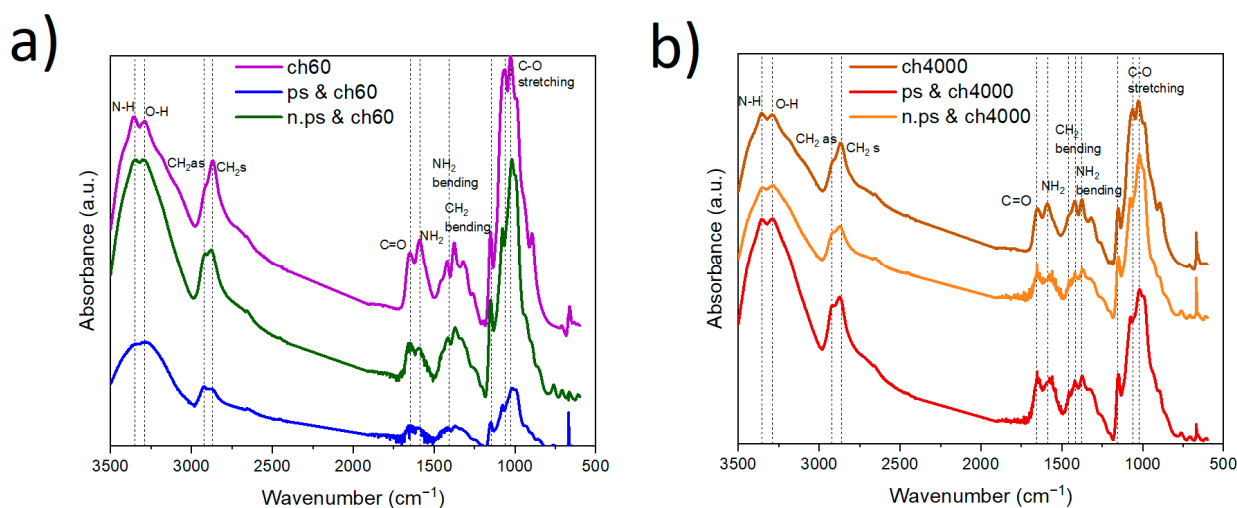


**Figure 2.** FTIR-Spectra of (a) ch60 (purple), ps & ch60 (blue), n.ps & ch60 (green), and (b) ch4000 (brown), ps & ch4000 (red), n.ps & ch4000 (orange). More information about the bonds is described in Table S1.

As deduced in Figure 1a, the presence of the band at  $1588\text{ cm}^{-1}$  is due to hydrogen bonding between the OH and  $\text{NH}_3^+$  of chitosan and the OH group of starch [14,31]. Both spectra of the ps blend with chitosan and n.ps mixed with chitosan are congruent to the native potato starch spectrum, which is already published in our previous work [9], indicating that the modification of potato starch with chitosan did not change the chemical structure. However, the OH stretching attributed to chitosan shows a slight shift to  $3320\text{ cm}^{-1}$ , and the peak related to the C=O of the amid I group at  $1588\text{ cm}^{-1}$  was shifted to  $1585\text{ cm}^{-1}$ , designating the presence of intermolecular hydrogen bonds ( $\text{O} \cdots \text{H-O}$  and  $\text{O} \cdots \text{H-N}$ ) between starch and chitosan [32].

The peak at  $1457\text{ cm}^{-1}$  corresponded to  $\text{CH}_2$  bending and the band at  $1417\text{ cm}^{-1}$  is related to the  $\text{CH}_2$  stretching as well as the C-O-O stretching. The occurrence of a narrow peak at  $1379\text{ cm}^{-1}$  indicated the  $\text{NH}_2$  bending (amide II). The bands around  $1000$  and  $900\text{ cm}^{-1}$  confirmed the skeletal vibrations corresponding to the CO stretching; the peak at  $655\text{ cm}^{-1}$  corresponded to the bending vibration of NH and OH [15].

Figure 3 illustrates the morphologies of the different samples used in the adsorption of iron and sulfate ions from water using SEM. Figure 3a displays the SEM image of ch60, which exhibits a smooth surface in comparison to Figure 3b of ps & ch60, and presents, as deduced in Figure 1, highly aggregated particles of chitosan and starch. Figure 3c of n.ps & ch60 reveals significant changes in the morphology of the examined particles, showing an inhomogeneous surface, with the disappearance of starch grains due to the existence of nano starch particles. This indicates that the modification of nano potato starch particles using ch60 was successful. Figure 3d presents the long chain chitosan ch4000, and Figure 3e of ps & ch4000 exhibits an inhomogeneous surface showing the presence of ps on the surface. Despite the high chain length of ch4000, the starch grains are clearly visible and not encapsulated with chitosan due to the large particle size of starch. Lastly, Figure 3f does

not reveal any significant changes. Both Figure 3e,f showed an inhomogeneous surface with the presence of aggregates; however, Figure 3f shows no starch.

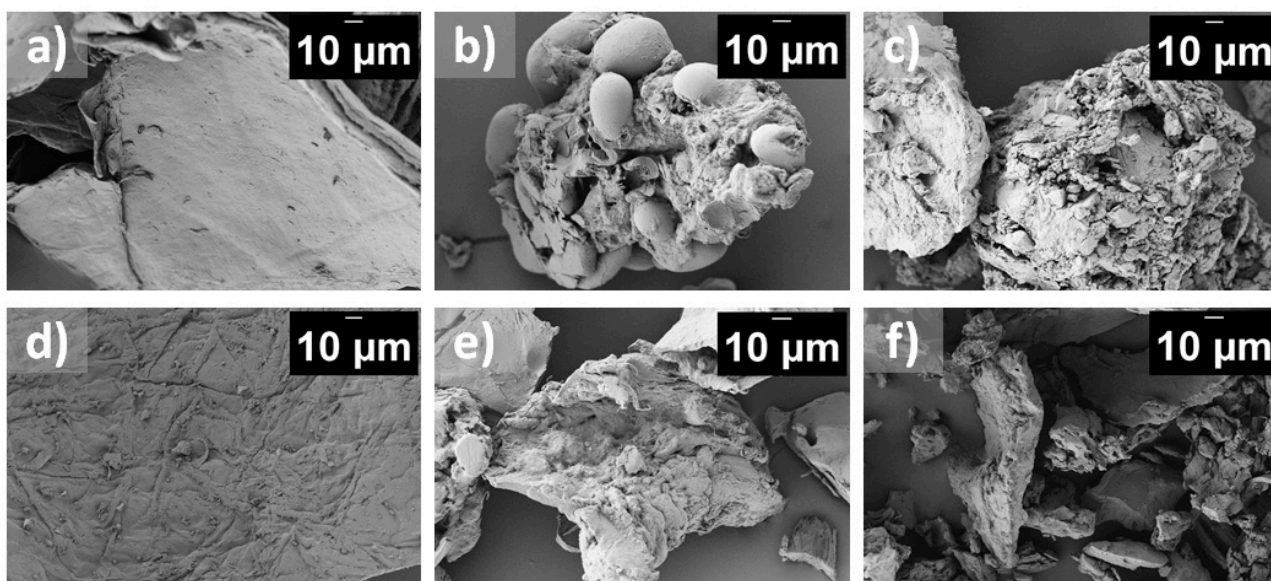


**Figure 3.** SEM measurements of (a) ch60, (b) ps & ch60, (c) n.ps & ch60, (d) ch4000, (e) ps & ch4000, (f) n.ps & ch4000.

In both Figure 3c,f, only chitosan is observed, suggesting that the chitosan was able to form intermolecular hydrogen bonds with nano starch. Starch is not shown in both Figures due to its very small size compared to chitosan. Moreover, to examine the surface property and determine the porosity of the samples, the sorption isotherms of  $N_2$  were measured. The studied samples showed no porous surface as showed in Figure S2 and Table S2, as the resulting surface area show no porosity due to the nature of these materials: both chitosan and starch in the native form before blending have no porous surface. By the blending process, chitosan and starch are both hydrophilic samples, and have a preference for water and can absorb moisture. This property can further decrease the possibility of pore formation on the surface since the materials can swell in contact with water, which leads to making the formation of porous impossible. Also, the SEM images are in agreement with these results and show no porosity.

The TGA analysis of samples was performed in a nitrogen environment and presented in Figure S3 showing almost the same curves of all the samples.

To examine the particle size distribution, laser diffractometry was used. The samples were added in powder form to the cell containing Milli-Q water, and were stirred for 2 min and then measured. The size distribution of the studied particles is depicted in Figure 4a. Both chitosans ch60 and ch4000 show almost the same particle size and exhibited a peak ranging from 200  $\mu m$  to 1000  $\mu m$ . The ps presented a narrow peak from 10  $\mu m$  to 100  $\mu m$ . Remarkably, when starch was added, the particle size distribution slightly decreased compared to the particle dimensions of both chitosans. Nevertheless, the particle size of the starch–chitosan blends is still high compared to starch. This indicates the presence of two components: starch and chitosan. Both ps & ch60 and n.ps & ch60 displayed a unimodal distribution characterized by a broad peak from 20  $\mu m$  to 1000  $\mu m$ . In contrast, ps & ch4000 and n.ps & ch4000 demonstrated a decrease of the particle size distribution compared to pure ch4000. The peak representing ps & ch4000 shifted, ranging from 60  $\mu m$  to 1000  $\mu m$ . The n.ps & ch4000 exhibited a narrow peak ranging from 40  $\mu m$  to 1000  $\mu m$ .

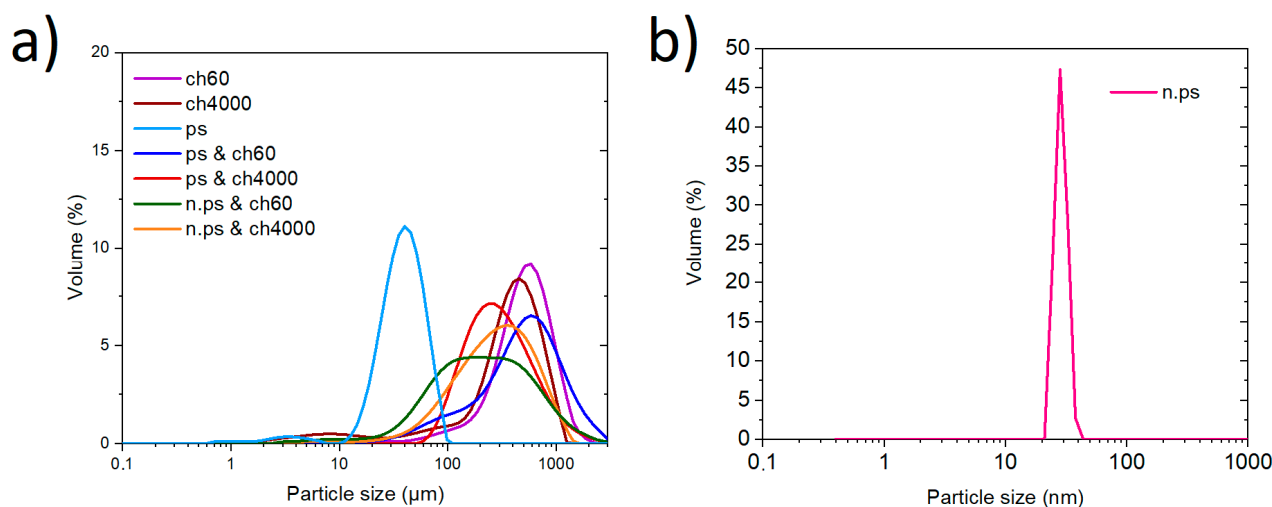


**Figure 4.** (a) Particle size distribution of ch60 (purple), ch4000 (brown), ps & ch60 (dark blue), ps & ch4000 (red), n.ps & ch60 (green), and n.ps & ch4000 (orange) was measured using the mastersizer 3000 in a dry state, and (b) the particle size of n.ps was measured using DLS in suspension. The intensity distribution and the volume distribution of n.ps are presented in Figure S4.

The distribution of the particle size of n.ps was measured using DLS. Figure 4b illustrated the particle size of n.ps. The n.ps exhibited a narrow peak from 20 nm to 50 nm. This indicates that the synthesis of n.ps from ps was successful.

After the sorption experiments, the adsorbers were dried under air at room temperature to study the distribution of elements onto the surface of the different particles. Afterward, they were examined using SEM-EDX. Figure 5 depicts the distribution of the elements of iron (represented in brown) and sulfur (represented in purple) on nano and native starch modified by chitosan particle surfaces after the sorption of  $\text{FeSO}_4$ . The chemical distribution analysis of both iron and sulfate ions is homogeneous over the same surface area of the particles, which indicates that the adsorption of iron and sulfate occurred simultaneously. Furthermore, the SEM-EDX analysis revealed a uniform distribution of iron and sulfur ions, indicating that the modified starch–chitosan blends have exhibited a strong attraction to both elements. This affinity can be linked to the existence of hydroxyl and amine groups on the particle surfaces.

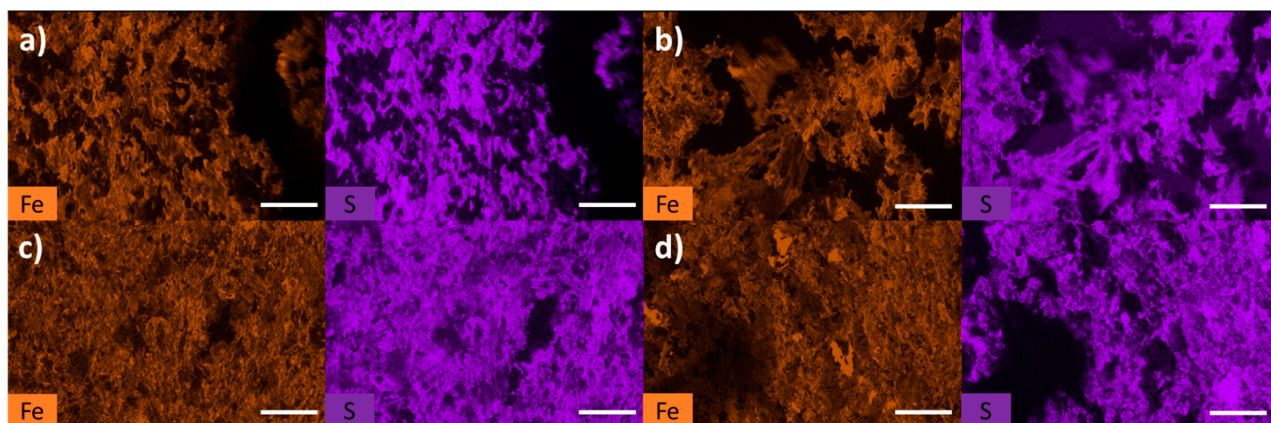


**Figure 5.** Elemental distribution of iron (brown) and sulfur (purple) at the surface of (a) ps & ch60, (b) n.ps & ch60, (c) ps & ch4000, and (d) n.ps & ch4000 after  $\text{FeSO}_4$  adsorption.

Table 3 displays the atomic concentration of iron and sulfur ions on the surface of the different samples. In conclusion, the results obtained from the sorption experiments and the subsequent SEM-EDX analysis indicate a uniform and simultaneous adsorption of  $\text{Fe}^{2+/3+}$  and  $\text{SO}_4^{2-}$  ions on the starch–chitosan particles' surface.

**Table 3.** Percent atomic concentration of iron and sulfur onto the surface area of ch60, ch4000, ps & ch60, ps & ch4000, n.ps & ch60, and n.ps & ch4000. The atomic concentration for the four used samples is presented in Supplementary Materials Figures S5–S12 and Tables S3–S10.

Atomic Concentration	Fe (%)	S (%)	Molar Ratio Fe:S
ps & ch60	2.9	1.2	2.4
ps & ch4000	5.04	1.58	3.18
n.ps & ch60	2.64	1.93	1.36
n.ps & ch4000	4.60	1.42	3.24

#### 4.2. Adsorption Kinetic

It is important to first study how adsorption changes in dependence of time before performing the adsorption isotherm experiment. Figure 6 presents the adsorption of iron ions (Figure 6a) and sulfate ions (b) onto the different four studied samples in dependence of time. The equilibrium of the adsorption was identified using the  $\text{FeSO}_4$  solution at a specific concentration of 1000 mg/L  $\text{Fe}^{2+/3+}$  and 1720 mg/L  $\text{SO}_4^{2-}$ . Due the uptake of iron ions, the samples transformed in color from white to a dark rusty brown. The intensity of the color increased in dependence of time, as observed in Figure S13. This change of the color could be explained by the oxidation of  $\text{Fe}^{2+}$  to  $\text{Fe}^{3+}$ , indicating that the samples successfully adsorbed  $\text{Fe}^{2+/3+}$ .

After 16 h, the adsorption equilibrium of all samples was reached. The increase of the adsorption capacity after 24 h is owed to the oxidation of iron, confirming that 24 h were sufficient for the adsorption equilibrium. Both n.ps & ch60 and n.ps & ch4000 show a high adsorption capacity for both  $\text{Fe}^{2+/3+}$  and  $\text{SO}_4^{2-}$  ions compared to ps & ch60 and ps & ch4000. Sulfate ions was adsorbed in larger amounts compared to iron ions. The adsorption capacity value of sulfate is almost two times higher compared to iron ions onto all the four adsorbers. This indicates that the negatively charged sulfate ions were firstly adsorbed and bound to the positively charged  $\text{NH}_3^+$  ions in aqueous media. And then, the adsorption of iron ions takes place.

To gain information about the adsorption rate and understand the adsorption process mechanism, both empirical models PFO and PSO were employed to fit the data for the kinetic parameters as observed in Figure 6a,b. The fitting parameters for  $\text{Fe}^{2+/3+}$  and  $\text{SO}_4^{2-}$  adsorption onto the different adsorbers for PFO and PSO are presented in Table 4. The PSO provided a better fit than the PFO based on the correlation coefficient ( $R^2$ ). The sulfate amount uptake is higher than the iron ions amount uptake, which confirms the results by the charge densities diagram. Due to the highly positive charged adsorber particles, it was easier to firstly adsorb  $\text{SO}_4^{2-}$  ions. Thus, the increase of sulfate ions onto the adsorbers raises the negative charge in the surface and makes it easier to adsorb the iron cations, which indicates that the adsorption is complementary.

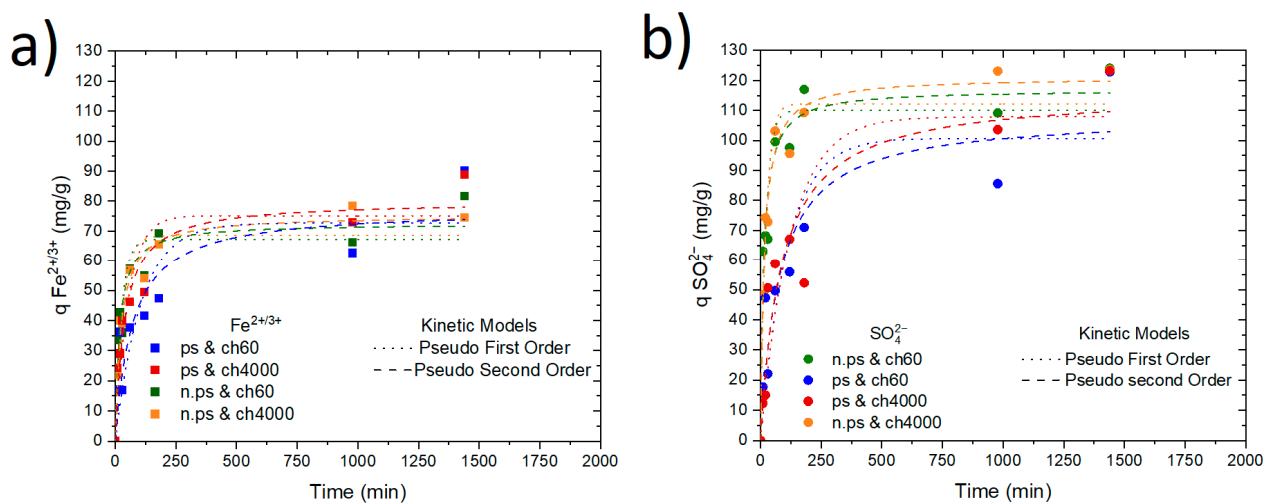


**Figure 6.** Adsorption efficiency of (a) iron ions at 1000 mg/L and (b) sulfate ions at 1720 mg/L from  $\text{FeSO}_4$  in dependence of time from 10 min to 24 h onto ps & ch60 (blue), ps & ch4000 (red), n.ps & ch60 (green), and n.ps & ch4000 (orange). Using 0.1 g of adsorbent comprising a 1:1 ratio of chitosan and starch at room temperature and  $\text{pH}_0$  4.26.

**Table 4.** Kinetic parameters established through PFO and PSO models for iron and sulfate ions onto the different studied adsorbents.

Kinetic Model Parameters	$\text{Fe}^{2+/3+}$						$\text{SO}_4^{2-}$					
	$q_{\text{eq}}$ (mg/g)	PFO K ( $\text{min}^{-1}$ )	$R^2$	$q_{\text{eq}}$ (mg/g)	PSO $K \times 10^{-4}$ (mg/g.min)	$R^2$	$q_{\text{eq}}$ (mg/g)	PFO K ( $\text{min}^{-1}$ )	$R^2$	$q_{\text{eq}}$ (mg/g)	PSO $K \times 10^{-4}$ (mg/g.min)	$R^2$
ps & ch60	72.70	0.009	0.771	77.45	1.83	0.837	100.72	0.009	0.822	108.34	1.20	0.851
ps & ch4000	75.11	0.018	0.862	80.03	3.30	0.935	107.91	0.008	0.835	116.09	1.00	0.891
n.ps & ch60	67.18	0.039	0.863	72.54	2.59	0.922	110.07	0.047	0.903	116.98	6.44	0.949
n.ps & ch4000	68.53	0.032	0.924	75.26	1.12	0.967	112.21	0.045	0.942	121.07	5.33	0.977

#### 4.3. Adsorption Isotherm

The adsorption isotherms of  $\text{Fe}^{2+/3+}$  and  $\text{SO}_4^{2-}$  on the four studied particles were investigated and illustrated in Figure 7. As mentioned in Section 4.2, after 24 h, the iron and sulfate ions have reached their adsorption equilibrium. Consequently, 24 h were fixed as the adsorption time for the samples.

The percentage adsorption isotherms of iron and sulfate ions on ch60 and ch4000 in dependence of the concentration of  $\text{FeSO}_4$  before the adsorption are illustrated in Figures S14 and S15. The initial  $\text{pH}_0$  and the equilibrium  $\text{pH}_{\text{eq}}$  values of adsorption of  $\text{FeSO}_4^{2-}$  onto ch60 and ch4000 are presented in Figure S16. As expected, the adsorption onto the four studied samples of  $\text{SO}_4^{2-}$  is higher than the adsorption of  $\text{Fe}^{2+/3+}$  due to the positive surface of the adsorbents. By observing the pH curve in Figure S18, it is noticeable that as the concentration of the  $\text{FeSO}_4$  solution increases, the pH value decreases, leading to the protonation of the amino group from  $\text{NH}_2$  to  $\text{NH}_3^+$ . This explains the binding of  $\text{SO}_4^{2-}$  to the protonated amino groups. Due to the binding of  $\text{SO}_4^{2-}$  ions to chitosan, a negative charge is generated, leading to the binding of cationic ions  $\text{Fe}^{2+/3+}$  through an electrostatic interaction [6]. The  $\text{pH}_0$  of the initial concentration of the  $\text{FeSO}_4$  solution is lower than the  $\text{pH}_{\text{eq}}$  values after adsorption, which indicates the bonding of iron and sulfate ions with the amino and the hydroxyl groups onto starch and chitosan blends. As the concentration of  $\text{FeSO}_4$  increased, there was a progressive reduction in pH until a plateau was achieved. Notably, this reduction in pH reached a plateau, suggesting that no further ions could be adsorbed. This plateau indicates the attainment of the adsorption's maximum capacity under the prevailing experimental conditions.

Remarkably, both n.ps & ch4000 and n.ps & ch60 demonstrated almost the same results: approximately 100% of iron and sulfate ions were removed at concentrations ranging from

the 0.5 mg/L to the 10 mg/L FeSO<sub>4</sub> solution (Figure S17). Afterwards, the concentration of Fe<sup>2+/3+</sup> from FeSO<sub>4</sub> gradually decreased until it reached a plateau at 20% by concentration ranges of 1500 mg/L and 2000 mg/L of Fe<sup>2+/3+</sup>, and concentration ranges of 2600 mg/L to 3550 mg/L of SO<sub>4</sub><sup>2-</sup> (Figure S17).

In Figure 7, the adsorption capacity on n.ps & ch4000 and n.ps & ch60 towards Fe<sup>2+/3+</sup> significantly increases until reaching plateaus at 115 mg/g and 80 mg/g, respectively. Figure 7b reveals a higher sulfate ions uptake on n.ps & ch4000 and n.ps & ch60 compared to iron ions, with values of 192 mg Fe<sup>2+/3+</sup>/g and 155 mg Fe<sup>2+/3+</sup>/g, respectively. This result can be attributed to the strong ionic interaction between sulfate ions and protonated NH<sub>3</sub><sup>+</sup> on the chitosan structure [33]. n.ps & ch4000 exhibits higher adsorption of both iron and sulfate ions compared to n.ps & ch60, which can be explained by the longer chain and higher molar mass of ch4000, resulting in a higher number of amine and hydroxyl groups that facilitate ion interaction and bonding with the adsorbers. Despite the NH<sub>2</sub> group's presence in the chitosan structure, the positive charge density is decreased due to the presence of the negatively charged nano starch, as shown in Figure 1. This indicates that both samples have more negatively charged OH groups, which facilitate the complexation of iron on n.ps & ch4000 and n.ps & ch60 compared to samples containing native potato starch. Moreover, due to the presence of weak ligand bases such as NH<sub>2</sub> and OH groups in the chemical structure of the adsorbers, the weak Lewis acids of Fe<sup>2+/3+</sup> form a stable complex with chitosan [34].

The adsorption of Fe<sup>2+/3+</sup> and SO<sub>4</sub><sup>2-</sup> ions onto ps & ch4000 and ps & ch60 is also high. As expected, the adsorption on ps & ch4000 is greater than on ps & ch60. From a concentration interval of 0.5 mg/L to 25 mg/L of FeSO<sub>4</sub> solution, more than 90% of Fe<sup>2+/3+</sup> and 70% of SO<sub>4</sub><sup>2-</sup> were removed (Figure S17 b), followed by a slow decrease until reaching plateaus of 15% and 13% at concentrations of 1572 mg/L Fe<sup>2+/3+</sup> and 3509 mg/L SO<sub>4</sub><sup>2-</sup>, respectively. The iron ions' uptake on ps & ch4000 and ps & ch60 significantly increases until reaching plateaus at 90 mg Fe<sup>2+/3+</sup>/g and 61 mg Fe<sup>2+/3+</sup>/g, respectively. Similarly, the metal uptake capacity of sulfate ions on ps & ch4000 and ps & ch60 significantly increases until reaching plateaus at 137 mg SO<sub>4</sub><sup>2-</sup>/g and 97 mg SO<sub>4</sub><sup>2-</sup>/g, respectively. Both the sulfate and iron ions show a low adsorption onto ps & ch4000 and ps & ch60 compared to n.ps & ch4000 and n.ps & ch60, due to the formation of agglomerate particles as presented in SEM-images, which makes the adsorption onto the adsorbers difficult.

Iron- and sulfate ions' uptake is, on the fourth studied samples, lower than onto ch4000 and ch60 (Figure S15); this could be explained by the interaction between the hydroxyl groups of starch and the amine groups of chitosan as mentioned Section 4.1 which reduce the adsorption of ions onto starch modified by chitosan.

To gain further insight into the adsorption type and process, the Langmuir, Sips, and Dubinin–Radushkevich models were used to model the adsorption isotherms of Fe<sup>2+/3+</sup> and SO<sub>4</sub><sup>2-</sup> ions, as described in our previous papers, for the purpose of maintaining consistency and comparability of the results [8,9]. The three fitting models are depicted in Figures S19–S21, and the fitting parameters are detailed in (Table 5, Table 6, Tables S11 and S12). According to Langmuir, the energy on the adsorption sites for homogeneous monolayer adsorption is equally distributed [23,35]. To determine heterogeneous adsorption, the Sips model, which combines Freundlich and Langmuir, was used to fit the adsorption isotherms depicted in Figure 7 [27]. Based on the Polanyi potential, Dubinin–Radushkevich distinguishes sorption types as either chemisorption or physisorption. Among the three fitted models, the Sips model exhibits the highest R<sup>2</sup> values (coefficient of determination) of the adsorption of Fe<sup>2+/3+</sup> on chitosan–starch particles. However, the Sips model exponent *n* for n.ps & ch60 and ps & ch60 presents values significantly higher than one, indicating a heterogeneity of the chitosan–starch surface. The Sips exponent *n* of ps & ch4000 and n.ps & ch4000 show values approximately of one; thus, Fe<sup>2+/3+</sup> on ps & ch4000 and n.ps & ch4000 could be better fitted using the Langmuir model, suggesting a single-layer adsorption [36]. The Sips model exhibits the highest R<sup>2</sup> for SO<sub>4</sub><sup>2-</sup> on the four adsorbers. Moreover, the *n<sub>s</sub>*

for n.ps & ch60 and ps & ch60 show values greater than one, leading to conclude that the adsorption is heterogenic.

Additionally, the calculated  $q_{max}$  values for both the  $Fe^{2+/3+}$  and  $SO_4^{2-}$  ions are similar to the experimental  $q_{max}$ . The calculated  $E_{ads,DR}$  values using the Dubinin–Radushkevich model show close similarity for all four studied adsorbents, indicating a similar affinity of the modified starch–chitosan samples towards  $Fe^{2+/3+}$  and  $SO_4^{2-}$ , despite the samples showing variations in their maximum metal uptake capacities. This observation can also be explained by the differences between nano and native ps modified with both chitosan types, as previously described.

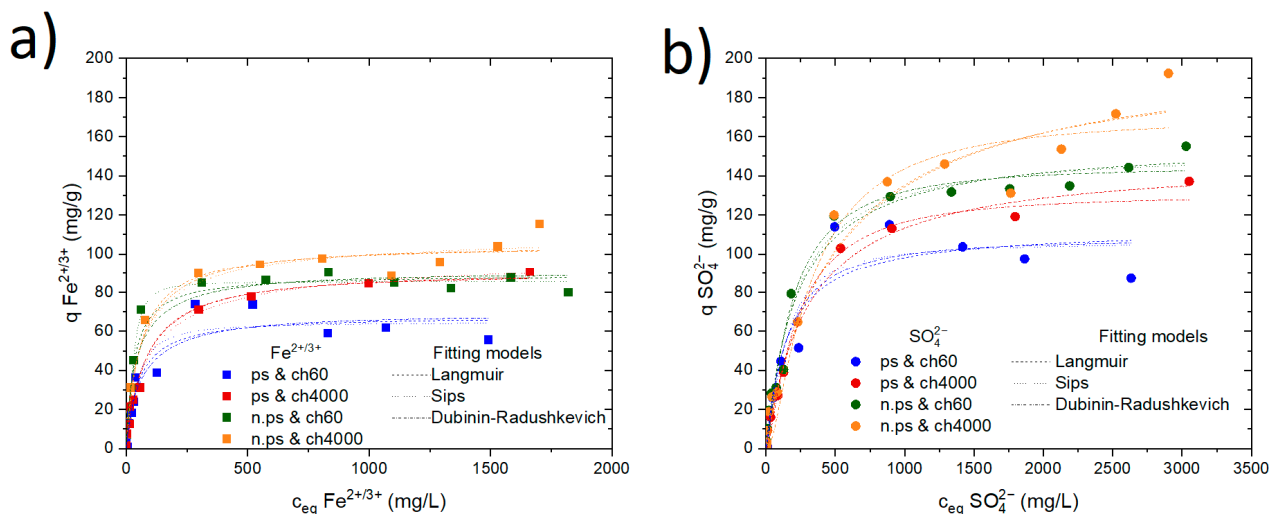


**Figure 7.** (a) Adsorption isotherms’ capacity for  $Fe^{2+/3+}$  from the  $FeSO_4$  solution along with corresponding the three different isotherm model fits: Langmuir, Sips, and Dubinin–Radushkevich. (b) Adsorption isotherms’ capacity for  $SO_4^{2-}$  from  $FeSO_4$  solution and the respective three different isotherm model fits: Langmuir, Sips, and Dubinin–Radushkevich. The corresponding  $pH_0$  and  $pH_{eq}$  values are presented in Figure S18. The Langmuir, Sips, and the Dubinin–Radushkevich fitting models were presented in Figures S19–S21. ps & ch60 (blue), ps & ch4000 (red), n.ps & ch60 (green), n.ps & ch4000 (orange). Tables S11 and S12 present the Fitting parameters. Using 0.1 g of adsorbent comprising a 1:1 ratio of chitosan and starch at room temperature.

**Table 5.** Fitting parameters for the adsorption of  $Fe^{2+}$  from the  $FeSO_4$  solution onto ps & ch60 (blue), ps & ch4000, n.ps & ch60, n.ps & ch4000 for Langmuir, Sips, and Dubinin–Radushkevich isotherm models.

Sample	Model	$Q_m$ (mg/g)	K (L/mg)	$\beta_{DR} \times 10^{-9}$ (mol <sup>2</sup> /J <sup>2</sup> )	N	$E_{ads,DR}$ (KJ/mol)	R <sup>2</sup> (COD)
ps & ch60	Langmuir	67.98	0.019	--	--	--	0.938
	Sips	64.60	0.006	--	1.35	--	0.944
	Dubinin–Radushkevich	68.26	--	13.2	--	61.5	0.933
ps & ch4000	Langmuir	91.65	0.013	--	--	--	0.990
	Sips	99.96	0.024	--	0.80	--	0.993
	Dubinin–Radushkevich	88.83	--	15.86	--	56.14	0.990
n.ps & ch60	Langmuir	89.05	0.031	--	--	--	0.983
	Sips	85.47	0.0034	--	1.72	--	0.995
	Dubinin–Radushkevich	89.79	--	10.51	--	68.94	0.972
n.ps & ch4000	Langmuir	104.98	0.017	--	--	--	0.981
	Sips	111.11	0.032	--	0.809	--	0.983
	Dubinin–Radushkevich	103.53	--	13.32	--	61.43	0.982

**Table 6.** Fitting parameters for the adsorption of  $\text{SO}_4^{2-}$  from the  $\text{FeSO}_4$  solution onto ps & ch60 (blue), ps & ch4000, n.ps & ch60, n.ps & ch4000 for Langmuir, Sips, and Dubinin–Radushkevich isotherm models.

Sample	Model	$Q_m$ (mg/g)	K (L/mg)	$\beta_{DR} \times 10^{-9}$ ( $\text{mol}^2/\text{J}^2$ )	N	$E_{ads,DR}$ (KJ/mol)	$R^2$ (COD)
ps & ch60	Langmuir	113.28	0.006	--	--	--	0.936
	Sips	106.26	0.0012	--	1.37	--	0.943
	Dubinin–Radushkevich	107.32	--	25.51	--	44.26	0.942
ps & ch4000	Langmuir	148.89	0.003	--	--	--	0.990
	Sips	148.04	0.0029	--	1.01	--	0.991
	Dubinin–Radushkevich	130.23	--	38.2	--	36.17	0.982
n.ps & ch60	Langmuir	157.49	0.004	--	--	--	0.987
	Sips	153.1	0.002	--	1.09	--	0.988
	Dubinin–Radushkevich	144.81	--	31.6	--	39.74	0.985
n.ps & ch4000	Langmuir	201.63	0.002	--	--	--	0.971
	Sips	207.50	0.002	--	0.95	--	0.970
	Dubinin–Radushkevich	169.54	--	56.3	--	29.79	0.963

## 5. Conclusions

In this article, we investigated the modification of native and nano starch using low molecular ch60 and high molecular ch4000. Additionally, we also tested their application as adsorbent materials for removing iron ions and the oxyanions sulfate from aqueous media. Particularly, we focused on examining the influence of chitosan chain length on the adsorption behaviors of iron and sulfate ions.

Our paper differs from most others in the field because of the novel, simple, and ecofriendly synthesis method we used to investigate how the chain length of chitosan influences the adsorption. Notably, we explored the modification of both native and nano starch using chitosan and examined the resulting effects. Furthermore, we are the first to report on the adsorption of  $\text{Fe}^{2+/3+}$  and  $\text{SO}_4^{2-}$  on starch modified using chitosan samples in an acidic pH range. The four synthesized particles were analyzed before their application on water treatment. As chitosan and starch were mixed, the charge density of ps & ch60, ps & ch4000, n.ps & ch60, and n.ps & ch4000 is decreased compared to ch60 and ch4000. The bonding between starch and chitosan was facilitated by hydrogen interactions between the OH and  $\text{NH}_3^+$  of chitosan and the OH group of starch. The adsorption kinetic was further investigated to investigate the adsorption equilibrium of the different adsorbents. The PFO and PSO were additionally examined; the most accurate fits are provided by the pseudo-PSO kinetic model for  $\text{Fe}^{2+/3+}$  and  $\text{SO}_4^{2-}$ . The adsorption of sulfate ions is usually by all particles higher as for  $\text{Fe}^{2+/3+}$  due to the existence of amino groups in the solution which facilitate the binding of the negatively charged  $\text{SO}_4^{2-}$  ions.

The adsorption of  $\text{Fe}^{2+/3+}$  can be explained by the presence of weak ligand bases such as the  $\text{NH}_2$  and OH groups in the chemical structure of the adsorbents, which facilitates the complexation with the weak Lewis acids of  $\text{Fe}^{2+/3+}$ . The adsorption isotherms were also fitted using Sips, Langmuir, and Dubinin–Radushkevich. The Sips model demonstrates the highest  $R^2$  values for the four samples. The Sips exponent n of ps & ch4000 and n.ps & ch4000 show values approximately of one; thus, the Langmuir model could provide a better fit for the adsorption of  $\text{Fe}^{2+/3+}$  on ps & ch4000 and n.ps & ch4000. The Sips model exhibits the highest  $R^2$  for  $\text{SO}_4^{2-}$  on the four adsorbents. Moreover, the  $n_s$  shows values nearly of one, leading to conclude that the adsorption is heterogenic.

**Supplementary Materials:** The following supporting information can be downloaded at: <https://www.mdpi.com/article/10.3390/polysaccharides4030019/s1>, References [8,19,34] are cited in supplementary material. Figure S1: Charge densities of the different studied particles in dependence of pH 3 and 5 of ch60 (purple), ch4000 (brown), ps & ch60 (dark blue), ps & ch4000 (red), n.ps & ch60 (green), and n.ps & ch4000 (orange) at (a) pH 1, and (b) pH 3; Figure S2: Nitrogen sorption isotherms at 77 K of (a) ch60 (purple), ch4000 (brown), (b) ps & ch60 (dark blue), ps & ch4000 (red),

(c) n.ps & ch60 (green), and n.ps & ch4000 (orange); Figure S3: Thermogravimetric analysis under  $N_2$  of ch60 (purple), ch4000 (brown), ps & ch60 (dark blue), ps & ch4000 (red), n.ps & ch60 (green), and n.ps & ch4000 (orange); Figure S4: Particle size measurement of n.ps (a) intensity distribution and (b) number distribution; Figure S5: (a) SEM images and SEM-EDX elemental mappings from ps & ch60, (b) sum spectrum; Figure S6: (a) SEM images and SEM-EDX elemental mappings from ps & ch4000, (b) sum spectrum; Figure S7: (a) SEM images and SEM-EDX elemental mappings from n. ps & ch60, (b) sum spectrum; Figure S8: (a) SEM images and SEM-EDX elemental mappings from n. ps & ch4000, (b) sum spectrum; Figure S9: (a) SEM images and SEM-EDX elemental mappings from ps & ch60, (b) sum spectrum at a concentration of  $Fe^{2+/3+}$  1000 mg/L; Figure S10: SEM images and SEM-EDX elemental mappings from ps & ch4000, (b) sum spectrum at a concentration of  $Fe^{2+/3+}$  1000 mg/L; Figure S11: SEM images and SEM-EDX elemental mappings from n.ps & ch60, (b) sum spectrum at a concentration of  $Fe^{2+/3+}$  1000 mg/L; Figure S12: SEM images and SEM-EDX elemental mappings from n.ps & ch4000, (b) sum spectrum at a concentration of  $Fe^{2+/3+}$  1000 mg/L; Figure S13: Change of color of samples at a concentration of iron 1000 mg/L and sulfate 1720 mg/L from  $FeSO_4$  in dependence of time from 10 min to 24 h onto (a) ps. & ch60, (b) ps & ch4000, (c) n.ps & ch60, and (d) n.ps & ch4000 at room temperature and  $pH_0$  4.26; Figure S14: (a) Percentage adsorption of  $Fe^{2+/3+}$  and (b) percentage adsorption of  $SO_4^{2-}$  from  $FeSO_4$  solution for ch60 (purple), and (b) ch4000 (brown); Figure S15: (a) Adsorption isotherm capacities for  $Fe^{2+/3+}$  and (b) Adsorption isotherms capacity for  $SO_4^{2-}$  from  $FeSO_4$  solution for ch60 (purple), and (b) ch4000 (brown); Figure S16: Corresponding  $pH_0$  and  $pH_{eq}$  values from adsorption of  $FeSO_4^{2-}$  onto (a) ch60 (purple), and (b) ch4000 (brown) with  $pH_0$  (grey) corresponds to the pH value of the adsorptive solution before the experiment and  $pH_{eq}$  corresponds to the pH value after the adsorption process; Figure S17: (a) Percentage adsorption of  $Fe^{2+/3+}$  and (b) percentage adsorption of  $SO_4^{2-}$  from  $FeSO_4$  solution with ps & ch60 (dark blue), ps & ch4000 (red), n.ps & ch60 (green), and n.ps & ch4000 (orange); Figure S18: Corresponding  $pH_0$  and  $pH_{eq}$  values from adsorption of  $FeSO_4^{2-}$  onto ps & ch60 (dark blue), ps & ch4000 (red), n.ps & ch60 (green), and n.ps & ch4000 (orange). With  $pH_0$  (grey) corresponds to the pH value of the adsorptive solution before the experiment and  $pH_{eq}$  corresponds to the pH value after the adsorption process; Figure S19: Adsorption isotherms capacity for (a)  $Fe^{2+/3+}$ , and (b)  $SO_4^{2-}$  from  $FeSO_4$  solution and the respective Langmuir isotherm fitting model; Figure S20: Adsorption isotherms capacity for (a)  $Fe^{2+/3+}$ , and (b)  $SO_4^{2-}$  from  $FeSO_4$  solution and the respective Sips isotherm fitting model; Figure S21: Adsorption isotherms capacity for (a)  $Fe^{2+/3+}$ , and (b)  $SO_4^{2-}$  from  $FeSO_4$  solution and the respective Dubinin–Radushkevich isotherm fitting model; Table S1: ATR-FTIR vibrations mode for chitosan–starch samples; Table S2: Surface area of the used samples using BET; Table S3: Percent atomic and weight concentrations of iron and sulfur onto the surface area of ps & ch60; Table S4: Percent atomic and weight concentrations of iron and sulfur onto the surface area of ps & ch4000; Table S5: Percent atomic and weight concentrations of iron and sulfur onto the surface area of n.ps & ch60; Table S6: Percent atomic and weight concentrations of iron and sulfur onto the surface area of n.ps & ch4000; Table S7: Percent atomic and weight concentrations of iron and sulfur onto the surface area of ps & ch60; Table S8: Percent atomic and weight concentrations of iron and sulfur onto the surface area of ps & ch4000; Table S9: Percent atomic and weight concentrations of iron and sulfur onto the surface area of n.ps & ch60; Table S10: Percent atomic and weight concentrations of iron and sulfur onto the surface area of n.ps & ch4000; Table S11: Fitting parameters for the adsorption of  $Fe^{2+}$  from  $FeSO_4$  solution onto ps & ch60 (blue), ps & ch4000, n.ps & ch60, n.ps & ch4000 for Langmuir, Sips, and Dubinin–Radushkevich isotherm models; Table S12: Fitting parameters for the adsorption of  $SO_4^{2-}$  from  $FeSO_4$  solution onto ps & ch60 (blue), ps & ch4000, n.ps & ch60, n.ps & ch4000 for Langmuir, Sips, and Dubinin–Radushkevich isotherm models. Table S13: Adsorption of iron ions onto biopolymers. Table S14: Adsorption of sulfate ions onto biopolymers.

**Author Contributions:** Methodology, C.S., R.B., N.G., C.B. and M.O. formal analysis, C.S., C.B. and R.B.; investigation, C.S. and R.B.; writing—original draft preparation, writing—review and editing, visualization, R.B., C.S. and S.S.; supervision, S.S. project administration, S.S.; funding acquisition S.S. All authors have read and agreed to the published version of the manuscript.

**Funding:** This research received no external funding.

**Institutional Review Board Statement:** Not applicable.

**Data Availability Statement:** All findings discussed are based on the data contained within this current study.

**Acknowledgments:** The authors thank the AGRANA Research and Innovation Center GmbH from Tulln, Austria, and Biolog Heppe GmbH from Landsberg, Germany for the support of the materials, discussions, and cooperativeness, and Eileen Schierz for the measurement of the elementary analysis.

**Conflicts of Interest:** The authors declare that the AGRANA Research and Innovation Center GmbH from Tulln, Austria, and Biolog Heppe GmbH from Landsberg, Germany provided material and technical support. They were not involved in the study design, collection, analysis, interpretation of data, the writing of this article or the decision to submit it for publication”.

## References

- Marsidi, N.; Abu Hasan, H.; Sheikh Abdullah, S.R. A Review of Biological Aerated Filters for Iron and Manganese Ions Removal in Water Treatment. *J. Water Process Eng.* **2018**, *23*, 1–12. [[CrossRef](#)]
- Rout, G.R.; Sahoo, S. Role of Iron in Plant Growth and Metabolism. *Rev. Agric. Sci.* **2015**, *3*, 1–24. [[CrossRef](#)]
- Geissler, C.; Singh, M. Iron, Meat and Health. *Nutrients* **2011**, *3*, 283–316. [[CrossRef](#)] [[PubMed](#)]
- Zak, D.; Hupfer, M.; Cabezas, A.; Jurasinski, G.; Audet, J.; Kleeberg, A.; McInnes, R.; Kristiansen, S.M.; Petersen, R.J.; Liu, H.; et al. Sulphate in Freshwater Ecosystems: A Review of Sources, Biogeochemical Cycles, Ecotoxicological Effects and Bioremediation. *Earth Sci. Rev.* **2021**, *212*, 103446. [[CrossRef](#)]
- Krasavtseva, E.; Gogoi, H.; Svetlov, A.; Leiviskä, T.; Makarov, D. Removal of Sulfate and Metals from Wastewater of a Mining Enterprise by a Dual Sorbent System: A Case Study. *Mine Water Environ.* **2023**, *42*, 200–208. [[CrossRef](#)]
- Weißpflog, J. Abtrennung von Schwermetall- und Oxyanionen aus wässrigen Lösungen mithilfe von Biopolymeren. Ph.D. Thesis, Technische Universität Dresden, Dresden, Germany, 2022.
- Apriyanto, A.; Compart, J.; Fettke, J. A Review of Starch, a Unique Biopolymer—Structure, Metabolism and in Planta Modifications. *Plant Sci.* **2022**, *318*, 111223. [[CrossRef](#)] [[PubMed](#)]
- Boughanmi, R.; Borchert, K.B.L.; Steinbach, C.; Mayer, M.; Schwarz, S.; Svirepa, A.; Schwarz, J.; Mertig, M.; Schwarz, D. Native and Oxidized Starch for Adsorption of Nickel, Iron, and Manganese Ions from Water. *Polysaccharides* **2022**, *3*, 556–573. [[CrossRef](#)]
- Borchert, K.B.L.; Boughanmi, R.; Reis, B.; Zimmermann, P.; Steinbach, C.; Graichen, P.; Svirepa, A.; Schwarz, J.; Boldt, R.; Schwarz, S.; et al. Removal of Lead, Cadmium, and Aluminum Sulfate from Simulated and Real Water with Native and Oxidized Starches. *Polysaccharides* **2021**, *2*, 429–453. [[CrossRef](#)]
- Lim, C.; Lee, D.W.; Israelachvili, J.N.; Jho, Y.; Hwang, D.S. Contact Time- and PH-Dependent Adhesion and Cohesion of Low Molecular Weight Chitosan Coated Surfaces. *Carbohydr. Polym.* **2015**, *117*, 887–894. [[CrossRef](#)]
- Weißpflog, J.; Steinbach, C.; Schwarz, D.; Schwarz, S. Simultaneous Adsorption of Iron and Sulfate Ions with Biopolymers. In Proceedings of the 2nd World Congress on Civil, Structural, and Environmental Engineering, Barcelona, Spain, 2–4 April 2017; pp. 2–5. [[CrossRef](#)]
- Weißpflog, J.; Boldt, R.; Kohn, B.; Scheler, U.; Jehnichen, D.; Tyrpekl, V.; Schwarz, S. Investigation of Mechanisms for Simultaneous Adsorption of Iron and Sulfate Ions onto Chitosan with Formation of Orthorhombic Structures. *Colloids Surf. A Physicochem. Eng. Asp.* **2020**, *592*, 124575. [[CrossRef](#)]
- Weißpflog, J.; Vehlouw, D.; Müller, M.; Kohn, B.; Scheler, U.; Boye, S.; Schwarz, S. Characterization of Chitosan with Different Degree of Deacetylation and Equal Viscosity in Dissolved and Solid State—Insights by Various Complimentary Methods. *Int. J. Biol. Macromol.* **2021**, *171*, 242–261. [[CrossRef](#)] [[PubMed](#)]
- Ramasubramaniam, S.; Govindarajan, C.; Nasreen, K.; Sudha, P.N. Removal of Cadmium (II) Ions from Aqueous Solution Using Chitosan/Starch Polymer Blend. *Compos. Interfaces* **2014**, *21*, 95–109. [[CrossRef](#)]
- Atangana, E.; Chiweshe, T.T.; Roberts, H. Modification of Novel Chitosan-Starch Cross-Linked Derivatives Polymers: Synthesis and Characterization. *J. Polym. Environ.* **2019**, *27*, 979–995. [[CrossRef](#)]
- Reis, B.; Gerlach, N.; Steinbach, C.; Carrasco, K.H.; Oelmann, M.; Schwarz, S.; Müller, M.; Schwarz, D. A Complementary and Revised View on the N-Acylation of Chitosan with Hexanoyl Chloride. *Mar. Drugs* **2021**, *19*, 385. [[CrossRef](#)] [[PubMed](#)]
- Wang, J.; Guo, X. Adsorption Kinetic Models: Physical Meanings, Applications, and Solving Methods. *J. Hazard. Mater.* **2020**, *390*, 122156. [[CrossRef](#)]
- Zhang, J. Physical Insights into Kinetic Models of Adsorption. *Sep. Purif. Technol.* **2019**, *229*, 115832. [[CrossRef](#)]
- Carrasco, K.H.; Höfgen, E.G.; Brunner, D.; Borchert, K.B.L.; Reis, B.; Steinbach, C.; Mayer, M.; Schwarz, S.; Glas, K.; Schwarz, D. Removal of Iron, Manganese, Cadmium, and Nickel Ions Using Brewers’ Spent Grain. *Polysaccharides* **2022**, *3*, 356–379. [[CrossRef](#)]
- Lagergren, S. Ueber Die Dämpfung Electricischer Resonatoren. *Ann. Der Phys.* **1898**, *300*, 290–314. [[CrossRef](#)]
- Ho, Y.S.; McKay, G. Pseudo-second order model for sorption processes. *Process Biochem.* **1999**, *34*, 451–465. [[CrossRef](#)]
- Gerente, C.; Lee, V.K.C.; Le Cloirec, P.; McKay, G. Application of Chitosan for the Removal of Metals from Wastewaters by Adsorption—Mechanisms and Models Review. *Crit. Rev. Environ. Sci. Technol.* **2007**, *37*, 41–127. [[CrossRef](#)]
- Langmuir, I. The Constitution and Fundamental Properties of Solids and Liquids. Part II.—Liquids. *J. Frankl. Inst.* **1917**, *184*, 721. [[CrossRef](#)]
- Sips, R. On the Structure of a Catalyst Surface. *J. Chem. Phys.* **1948**, *16*, 490–495. [[CrossRef](#)]
- Dubinin, M. The Equation of the Characteristic Curve of Activated Charcoal. *Proc. USSR Acad. Sci.* **1947**, *55*, 327–329.

26. Song, X.; Zhang, Y.; Yan, C.; Jiang, W.; Chang, C. The Langmuir Monolayer Adsorption Model of Organic Matter into Effective Pores in Activated Carbon. *J. Colloid Interface Sci.* **2013**, *389*, 213–219. [[CrossRef](#)]
27. Foo, K.Y.; Hameed, B.H. Insights into the Modeling of Adsorption Isotherm Systems. *Chem. Eng. J.* **2010**, *156*, 2–10. [[CrossRef](#)]
28. Maciel, V.B.V.; Yoshida, C.M.P.; Franco, T.T. *Chitosan/Pectin Polyelectrolyte Complex as a PH Indicator*; Elsevier Ltd.: Amsterdam, The Netherlands, 2015; Volume 132, ISBN 5519404364.
29. Dang, K.M.; Yoksan, R. Development of Thermoplastic Starch Blown Film by Incorporating Plasticized Chitosan. *Carbohydr. Polym.* **2015**, *115*, 575–581. [[CrossRef](#)]
30. Jiménez-Regalado, E.J.; Caicedo, C.; Fonseca-García, A.; Rivera-Vallejo, C.C.; Aguirre-Loredo, R.Y. Preparation and Physicochemical Properties of Modified Corn Starch–Chitosan Biodegradable Films. *Polymers* **2021**, *13*, 4431. [[CrossRef](#)]
31. Xu, Y.X.; Kim, K.M.; Hanna, M.A.; Nag, D. Chitosan-Starch Composite Film: Preparation and Characterization. *Ind. Crops Prod.* **2005**, *21*, 185–192. [[CrossRef](#)]
32. Jiang, S.; Yu, Z.; Hu, H.; Lv, J.; Wang, H.; Jiang, S. Adsorption of Procyanidins onto Chitosan-Modified Porous Rice Starch. *Lwt* **2017**, *84*, 10–17. [[CrossRef](#)]
33. Schwarz, S.; Steinbach, C.; Schwarz, D.; Mende, M.; Boldt, R. Chitosan—The Application of a Natural Polymer against Iron Hydroxide Deposition. *Am. J. Anal. Chem.* **2016**, *07*, 623–632. [[CrossRef](#)]
34. Weißpflog, J.; Gündel, A.; Vehlouw, D.; Steinbach, C.; Müller, M.; Boldt, R.; Schwarz, S.; Schwarz, D. Solubility and Selectivity Effects of the Anion on the Adsorption of Different Heavy Metal Ions onto Chitosan. *Molecules* **2020**, *25*, 2482. [[CrossRef](#)] [[PubMed](#)]
35. Al-Ghouti, M.A.; Da'ana, D.A. Guidelines for the Use and Interpretation of Adsorption Isotherm Models: A Review. *J. Hazard. Mater.* **2020**, *393*, 122383. [[CrossRef](#)] [[PubMed](#)]
36. Wang, J.; Guo, X. Adsorption Isotherm Models: Classification, Physical Meaning, Application and Solving Method. *Chemosphere* **2020**, *258*, 127279. [[CrossRef](#)] [[PubMed](#)]

**Disclaimer/Publisher's Note:** The statements, opinions and data contained in all publications are solely those of the individual author(s) and contributor(s) and not of MDPI and/or the editor(s). MDPI and/or the editor(s) disclaim responsibility for any injury to people or property resulting from any ideas, methods, instructions or products referred to in the content.